China Ocean Eng., 2017, Vol. 31, No. 1, P. 1–10
DOI: 10.1007/s13344-017-0001-x, ISSN 0890-5487
http://www.chinaoceanengin.cn/ E-mail: coe@nhri.cn

Tension and Drag Forces of Flexible Risers Undergoing Vortex-Induced Vibration

SONG Lei-jian[a, b], FU Shi-xiao[a, b, *], LI Man[c], GAO Yun[d], MA Lei-xin[a]

[a]State Key Laboratory of Ocean Engineering, Shanghai Jiao Tong University, Shanghai 200240, China

[b]Collaborative Innovation Center for Advanced Ship and Deep-Sea Exploration, Shanghai 200240, China

[c]Marine Design & Research Institute of China, Shanghai 200011, China

[d]State Key Laboratory of Oil and Gas Reservoir Geology and Exploration, Southwest Petroleum University, Chengdu 610500, China

Received June 29, 2015; revised December 14, 2015; accepted January 12, 2016

Abstract

This paper presents the results of an experimental investigation on the variation in the tension and the distribution of drag force coefficients along flexible risers under vortex-induced vibration (VIV) in a uniform flow for Reynolds numbers (*Re*) up to 2.2×10^5. The results show that the mean tension is proportional to the square of the incoming current speed, and the tension coefficient of a flexible riser undergoing VIV can be up to 12. The mean drag force is uniformly and symmetrically distributed along the axes of the risers undergoing VIV. The corresponding drag coefficient can vary between 1.6 and 2.4 but is not a constant value of 1.2, as it is for a fixed cylinder in the absence of VIV. These experimental results are used to develop a new empirical prediction model to estimate the drag force coefficient for flexible risers undergoing VIV for Reynolds number on the order of 10^5, which accounts for the effects of the incoming current speed, the VIV dominant modal number and the frequency.

Key words: flexible riser, drag force, tension force, vortex-induced vibration

Citation: Song, L. J., Fu, S. X., Li, M., Gao, Y., Ma, L. X., 2017. Tension and drag forces of flexible risers undergoing vortex-induced vibration. China Ocean Eng., 31(1): 1–10, doi: 10.1007/s13344-017-0001-x

1 Introduction

An incoming flow generates hydrodynamic forces on flexible risers. These forces typically consist of a drag force in the in-line direction (IL) and a lift force in the cross-flow direction (CF). The lift force exhibits periodic oscillations around a zero mean and results in the VIV of the flexible risers in the CF direction. The drag force can be divided into a periodic oscillating drag force and a mean drag force. The periodic oscillating force causes the riser to vibrate with a high frequency and small amplitude, i.e., VIV in the IL direction. For flexible riser, VIV in the CF and IL direction can lead to rapid accumulation of fatigue damage, and the issue of VIV has been studied in depth over the last three decades (Li et al., 2011; Tognarelli et al., 2004; Fang, 2013; Fu et al., 2013a, 2013b; Niedzwecki and Fang, 2013; Fang et al., 2014; Gao et al., 2014; Wang et al., 2014a, 2014b, 2015). The mean drag force leads to steady deformation with a relatively large amplitude of the riser, which affects whether the structural strength of the riser meets the design criteria (Summer and Fredsoe, 2006). Hence, it is critical to determine the mean drag force acting on the riser to analyze the global dynamic response of the riser system. An in-depth understanding of the characteristics of the mean drag force is essential for effective structural design. The Morison equation is usually used to calculate the mean drag forces on risers in their strength and safety design. A drag coefficient of 1.2 is currently used in most specifications for a rigid cylinder being towed in a tank. Recent studies have shown that VIV can significantly amplify the mean drag forces on flexible risers, resulting in a drag coefficient that is generally larger than 1.2 (Vandiver, 1983; de Wilde and Huijsmans, 2004; Chaplin et al., 2005). Therefore, it is important to investigate into the mean drag force in the presence of VIV and the amplification of VIV on drag coefficient in the design of deep water risers. In addition, in the design of top-tensioned risers, flexible risers, and umbilicals, axial tension is a very important design parameter that determines the natural frequencies, stress distributions, VIV predictions, and compensators. Thus, accurate prediction of the riser's axial tension under VIV is also highly significant.

Both numerical simulations and model tests have been used to study the hydrodynamic characteristics of flexible

Foundation item: This research was financially supported by the National Natural Science Foundation of China (Grant No. 51490674).
*Corresponding author. E-mail: shixiao.fu@sjtu.edu.cn

risers under VIV. In numerical simulations, computational fluid dynamics (CFD) has been used to calculate the fluid forces by dividing the flexible riser into a large number of rigid segments and assuming that the flow along each segment is two-dimensional. Willden and Graham (2001) used a vortex method with a hybrid formula to examine the fluid–structure interactions of marine risers. Yamamoto et al. (2005) developed a quasi-3D model to investigate into the hydroelastic interactions between oscillating flexible cylinders and estimated the hydrodynamic forces using a discrete vortex method. Evangelinos et al. (2000) used direct numerical simulation (DNS) based on spectral elements to simulate 3D flow past rigid and flexible cylinders and calculated the hydrodynamic forces acting on a flexible cylinder. However, these numerical calculations have not been verified against benchmark experiments. In model testing, it is challenging to directly measure the drag force on a riser under a current; thus, researchers often measure the total drag force by mounting force sensors at the ends of the models (Vandiver, 1983; Chaplin et al., 2005; Baarholm et al., 2007; Fu et al., 2011). Besides, Huera-Huarte et al. (2006, 2009) determined the fluid forces by using displacement measurements at various sites as the input to a finite element analysis of a vertically tensioned riser that was exposed to a stepped current.

Vandiver (1983) experimentally investigated into the VIV amplification of the drag coefficient for a flexible riser and found that the drag coefficient depends nonlinearly on the root mean square of VIV displacement in the CF direction (Y_{RMS}). Blevins (1990) reported that the drag coefficient depended linearly on Y_{RMS}. Chaplin et al. (2005) found that the mean drag coefficient was a quadratic function of the standard deviation of the VIV displacement in the CF direction on a flexible riser in a stepped current in model tests. However, in the aforementioned studies, the largest Reynolds number investigated was only on the order of 10^4, whereas in practical situations, risers are subjected to Reynolds number on the order of 10^5 or more. Because the flow characteristics and the flow separation modes depend strongly on Reynolds number, the performance of drag force and VIV of the risers under high Reynolds number will be different from those under low Reynolds number. Thus, further studies are required to determine whether the test results for $Re<10^4$ are representative of the VIV amplification on the drag coefficient at higher Reynolds number.

In the present study, four pre-tensioned flexible riser models are used to investigate the tension and mean drag forces under VIV in a uniform flow. Reynolds numbers up to 2×10^5 are investigated. In the tests, the strains are measured on the incident flow and downstream surfaces of the models. The values of the measured strain are used to derive the mean tension and mean drag force under different currents. The mean drag force is calculated at different positions of the models using beam-bending theory, and the drag coefficient distribution is investigated as a function of Reynolds number. The test results are then used to formulate an empirical equation for estimating the drag coefficient of flexible risers under VIV conditions.

2 Experimental apparatus

The experiments are carried out in a towing tank that is 192 m long, 10 m wide and 4.2 m deep. The riser model is horizontally installed on a towing carriage at a water depth of 1.5 m. A uniform flow is simulated by towing the riser at a constant speed. Fig. 1 is a schematic of the test apparatus. The two ends of the riser model are pin connected to the end devices through universal joints, which can free the bending in IL and CF directions of the model but prevent any torsional motions along the axis of the model. The end devices can apply a constant pre-tension to the riser model, where the pre-tension range over all the tests performed is 872–4905 N.

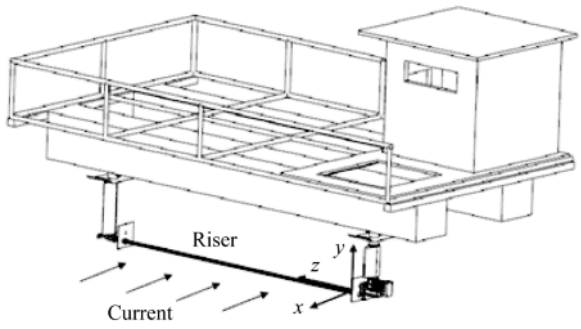

Fig. 1. Schematic of test apparatus.

Four riser models are used in the experiments. The properties of these models are listed in Table 1. In order to investigate the performance of tension and drag force of the flexible risers undergoing VIV under high Reynolds number, Model 4 was fabricated by bundling the cylindrical rubber onto a core steel pipe, which will increase the model hydrodynamic diameter to the full scale dimension and therefore high Reynolds number, meanwhile keep the model to be flexible enough to be excited into vibrations (Fu et al., 2011).

To simulate the real vibration characteristics of the risers, the pre-tension chosen for the model tests in Table 1 is determined by requiring that the vibration of the model be dominated by the tension instead of the bending stiffness, i.e., the pre-tension is larger than the Euler force. Furthermore, a small pre-tension may result in extremely large deflections under the drag force on the riser model, whereas an extremely large pre-tension can significantly increase the natural frequencies of the model such that significantly higher towing speeds are required to induce VIV and deflections.

Four groups of Fiber Bragg Grating (FBG) strain sen-

Table 1 Properties of riser models

	Model 1	Model 2	Model 3	Model 4
Outer diameter (m)	0.020	0.030	0.030	0.051
Wall thickness (m)	0.0010	0.0015	0.0015	0.0035
Hydrodynamic diameter (m)	0.0210	0.0310	0.0310	0.1683
Length (m)	5.27	7.90	7.90	7.90
Density (kg/m^3)	8900	8900	8900	7900
Bending stiffness (N·m^2)	291.71	1476.76	1476.76	31101.38
Mass ratio	2.50	2.50	2.50	0.84
Length/diameter ratio	2630	2630	2630	154.9
Pre-tension (N)	872	1962	2943	4905

sors are arranged along the IL and CF directions on the model's surface to obtain the strain of the riser models during experiments, as shown in Fig. 2. The FBG strain sensors at locations IL1 and IL2 are symmetric with respect to the neutral layer of the model in the IL direction and are used to measure the strains ε_{IL1} and ε_{IL2}, while the strain sensors at the locations CF1 and CF2 measure the strains ε_{CF1} and ε_{CF2}. The numbers of FBG strain sensors used in the CF and IL directions for each model are summarized in Table 2. The strain sensors were uniformly distributed along the axis of the model, and the spacing between adjacent sensors for each model is listed in Table 2. The signals are sampled at 250 Hz.

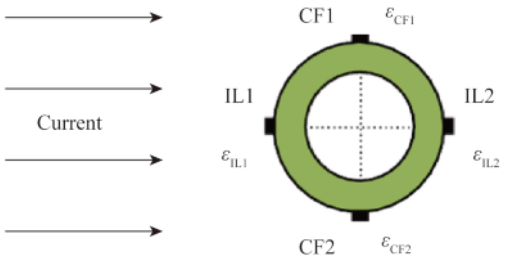

Fig. 2. Schematic of FBG strain sensors located on the model cross section.

Table 2 Number and spacing of FBG strain sensors in the CF and IL directions for each model

Model No.	CF		IL	
	Sensor number	Sensor spacing (m)	Sensor number	Sensor spacing (m)
1	13	0.42	19	0.28
2 & 3	19	0.42	37	0.21
4	9	0.90	9	0.90

3 Data analysis

3.1 Mean drag force and drag coefficient

Fig. 3a shows a flexible riser under a pre-tension (T_0), where the riser's axis lies along the z-axis and is perpendicular to the incoming flow along the x-axis. The IL plane for the riser is the xOz plane of the coordinate system, and the CF plane is the yOz plane. The total drag force at point z on the riser in the IL plane can be expressed as:

$$F_D(z,t) = \bar{F}_{md}(z) + F_{vivd}(z,t), \quad (1)$$

where $F_D(z,t)$ is the total drag force at point z on the riser at time t; $\bar{F}_{md}(z)$ is the local mean drag force at point z and is a time-independent and position-dependent constant; and $F_{vivd}(z,t)$ is the local periodic oscillating drag force at point z that varies periodically with time.

The action of $\bar{F}_{md}(z)$ results in a steady bending deformation in the IL plane on the riser that does not change with time. The position of the riser corresponding to the steady deformation is called the equilibrium position. The dynamic drag force $F_{vivd}(z,t)$ causes the riser to vibrate periodically around the equilibrium position, corresponding to the VIV in the IL plane (VIV_IL) that is shown in Fig. 3b.

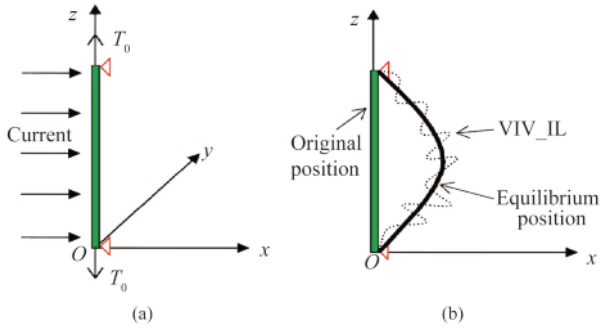

Fig. 3. Schematic of steady bending deformation and VIV in the IL plane of a flexible riser.

In this study, the riser model is hinged at both ends and subjected to pre-tension. Thus, the steady bending deformation induced by $\bar{F}_{md}(z)$ can be regarded as the complex bending of a beam, as shown in Fig. 4.

From beam-bending theory, the governing equation for the steady bending deformation can be expressed as (Chen and Chen, 1984):

$$EI\frac{\partial^4 w(z)}{\partial z^4} - \overline{T}\frac{\partial^2 w(z)}{\partial z^2} = \bar{F}_{md}(z), \quad (2)$$

where EI is the bending stiffness of the riser, $w(z)$ is the displacement from the steady bending deformation at point z, and $\overline{T}$ is the mean tension at the two ends of the riser. Although the tension of the riser model changes periodically in the presence of VIV, the steady bending deformation that is induced by the mean drag force does not change with time,

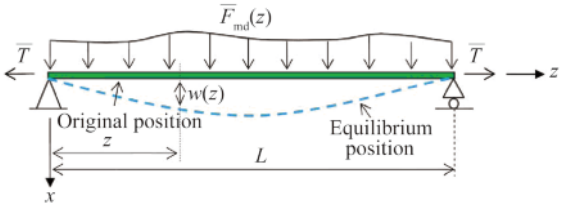

Fig. 4. Steady bending deformation induced by the mean drag force of the riser model.

such that the tension can be described as $\overline{T}$.

From beam-bending theory, the relationship between the displacement and the corresponding bending strain can be expressed as:

$$\frac{\partial^2 w(z)}{\partial z^2} = -\frac{\overline{\varepsilon}_{\mathrm{mb}}(z)}{R}, \tag{3}$$

where R is the radius of the riser, and $\overline{\varepsilon}_{\mathrm{mb}}(z)$ is the mean bending strain at point z that is caused by the steady bending deformation, which is a time-independent and position-dependent constant. Differentiating Eq. (3) twice yields,

$$\frac{\partial^4 w(z)}{\partial z^4} = -\frac{1}{R}\frac{\partial^2 \overline{\varepsilon}_{\mathrm{mb}}(z)}{\partial z^2}. \tag{4}$$

Substituting Eqs. (3) and (4) into Eq. (2) yields,

$$-\frac{EI}{R}\frac{\partial^2 \overline{\varepsilon}_{\mathrm{mb}}(z)}{\partial z^2} + \frac{\overline{T}}{R}\overline{\varepsilon}_{\mathrm{mb}}(z) = \bar{F}_{\mathrm{md}}(z). \tag{5}$$

For a riser model with a hydrodynamic diameter of D, $\bar{F}_{\mathrm{md}}(z)$ can be expressed as (API RP 2RD, 1998):

$$\bar{F}_{\mathrm{md}}(z) = \frac{1}{2}\rho C_{\mathrm{d}}(z) D V|V|, \tag{6}$$

where $C_{\mathrm{d}}(z)$ is the drag coefficient at point z of the riser model, ρ is the fluid density, and V is the fluid velocity. The form of the $V|V|$ term indicates that the drag force acts in the same direction as the incoming current.

If the axial distribution of $\bar{F}_{\mathrm{md}}(z)$ is known, Eq. (6) can be used to derive $C_{\mathrm{d}}(z)$ at different cross-sections, which can then be averaged over the length to obtain the mean drag coefficient ($\overline{C}_{\mathrm{d}}$):

$$C_{\mathrm{d}}(z) = \frac{2\bar{F}_{\mathrm{md}}(z)}{\rho D V|V|}; \tag{7}$$

$$\overline{C}_{\mathrm{d}} = \frac{1}{L}\int_0^L C_{\mathrm{d}}(z)\mathrm{d}z, \tag{8}$$

where L is the length of the riser model.

3.2 Mean bending strain

In the model tests, the strains on the incident flow surface [$\varepsilon_{\mathrm{IL1}}(z, t)$] and the downstream surface [$\varepsilon_{\mathrm{IL2}}(z, t)$] at IL1 and IL2 that are measured using FBG strain sensors can be expressed as:

$$\begin{cases} \varepsilon_{\mathrm{IL1}}(z,t) = \overline{\varepsilon}_{\mathrm{mb}}(z) + \varepsilon_{\mathrm{vivb}}(z,t) + \varepsilon_{\mathrm{T}}(z,t) \\ \varepsilon_{\mathrm{IL2}}(z,t) = -\overline{\varepsilon}_{\mathrm{mb}}(z) - \varepsilon_{\mathrm{vivb}}(z,t) + \varepsilon_{\mathrm{T}}(z,t) \end{cases} \tag{9}$$

where $\overline{\varepsilon}_{\mathrm{mb}}(z)$ is the mean bending strain at point z that is induced by the steady bending deformation; $\varepsilon_{\mathrm{vivb}}(z, t)$ is the dynamic strain induced by the VIV, and $\varepsilon_{\mathrm{T}}(z, t)$ is the strain induced by the axial tension. Eq. (9) can be re-arranged to yield,

$$\overline{\varepsilon}_{\mathrm{mb}}(z) = \frac{\varepsilon_{\mathrm{IL1}}(z,t) - \varepsilon_{\mathrm{IL2}}(z,t)}{2} - \varepsilon_{\mathrm{vivb}}(z,t); \tag{10}$$

$$\varepsilon_{\mathrm{T}}(z,t) = \frac{\varepsilon_{\mathrm{IL1}}(z,t) + \varepsilon_{\mathrm{IL2}}(z,t)}{2}. \tag{11}$$

Because the VIV in the IL direction is a periodic oscillation around the equilibrium position, $\varepsilon_{\mathrm{vivb}}(z, t)$ is also periodic. In addition, for a signal sampling frequency above 100 Hz, the duration for sampling steady data and the incoming flow is considerably longer than one VIV period. Therefore, the time-averaged strain $\left[\overline{\varepsilon_{\mathrm{vivb}}(t,z)}\right]$ induced by the VIV should be zero, i.e.

$$\overline{\varepsilon_{\mathrm{vivb}}(t,z)} = 0. \tag{12}$$

Averaging Eq. (10) over time and substituting Eq. (12) into Eq. (10) yield

$$\overline{\varepsilon}_{\mathrm{mb}}(z) = \frac{\overline{\varepsilon_{\mathrm{IL1}}(z,t) - \varepsilon_{\mathrm{IL2}}(z,t)}}{2}. \tag{13}$$

The analysis presented above is used to calculate the strain in the incident flow surface ($\varepsilon_{\mathrm{IL1}}$), the mean bending strain ($\overline{\varepsilon}_{\mathrm{mb}}$), the strain induced by the VIV ($\varepsilon_{\mathrm{vivb}}$), and the strain induced by the axial tension (ε_{T}) at 2.69 m in Model 3, which are shown in Fig. 5.

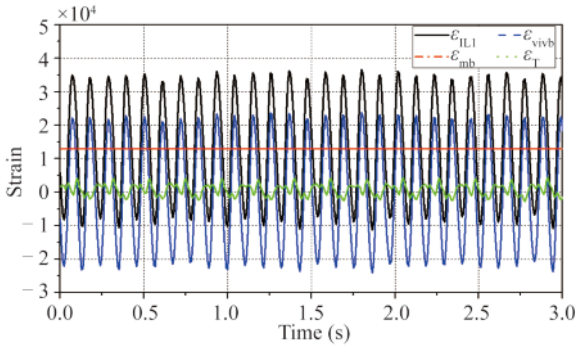

Fig. 5. Strains $\varepsilon_{\mathrm{IL1}}$, $\overline{\varepsilon}_{\mathrm{mb}}$, $\varepsilon_{\mathrm{vivb}}$ and ε_{T} at 2.69 m in Model 3.

3.3 Mean tension

For a riser model that is hinged at two ends with a pre-tension force (T_0), the axial tension varies under flow. The strain induced by the axial tension is given by Eq. (11). According to the beam theory, the axial tension can be calculated as:

$$T(z,t) = \frac{EA}{2}\left[\varepsilon_{\mathrm{IL1}}(z,t) + \varepsilon_{\mathrm{IL2}}(z,t)\right], \tag{14}$$

where EA is the tensile stiffness of the riser model. The mean tension ($\overline{T}$) can be obtained by averaging the axial tension both in space and time:

$$\overline{T} = \frac{EA}{2L}\int_0^L \overline{\left[\varepsilon_{\mathrm{IL1}}(z,t) + \varepsilon_{\mathrm{IL2}}(z,t)\right]}\ \mathrm{d}z. \tag{15}$$

4 Results and discussion

4.1 Mean tension and tension coefficient

For Model 4, two three-component force transducers are used at the ends of the model to measure the axial tension, from which $\overline{T}$ can be directly obtained. The mean tension ($\overline{T}$) for Model 4 that is calculated using Eq. (15) and the corresponding measurements under different current speeds are shown in Fig. 6. There is a good agreement between the cal-

culated and measured values, with a maximum relative error of 2.665% .This confirms the reliability of the method used to calculate $\overline{T}$ for the models.

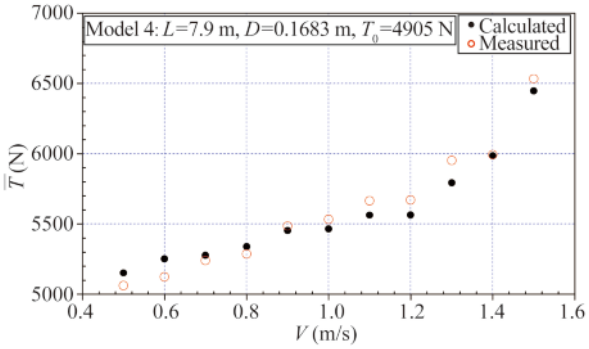

Fig. 6. Mean tension under different current speeds for Model 4.

Fig. 7 shows $\overline{T}$ as a function of current speed for Models 1–4. The mean tension ($\overline{T}$) increases with current speed for each model, and $\overline{T}$ increases more slowly at low current speeds than at high speeds. The least-squares fitting results in Fig. 7 show that $\overline{T}$ is approximately proportional to the square of the current speed over the entire speed range. However, some outliers can be observed in Fig. 7. Re-testing the cases corresponding to the outliers produces the same results. But we have not been able to explain the reason for these results; thus, further research is required.

During the tests, a constant pre-tension (T_0) is imposed at the model's ends; thus, $\overline{T}$ consists of T_0 and the increment in the mean tension ($\Delta\overline{T}$) that is induced by the VIV on the riser:

$$\overline{T} = T_0 + \Delta\overline{T}. \tag{16}$$

Thus, $\Delta\overline{T}$ can be obtained as:

$$\Delta\overline{T} = \overline{T} - T_0. \tag{17}$$

Fig. 8 shows ($\Delta\overline{T}$) as a function of the current speed for Models 1–4. ($\Delta\overline{T}$) is clearly proportional to the square of the current speed. For Models 2 and 3, which have the same hydrodynamic diameters but different pre-tension forces, ($\Delta\overline{T}$) is essentially the same at the same current speed. For Models 1, 2 and 4, the larger the hydrodynamic diameter is, the larger ($\Delta\overline{T}$) is at the same current speed.

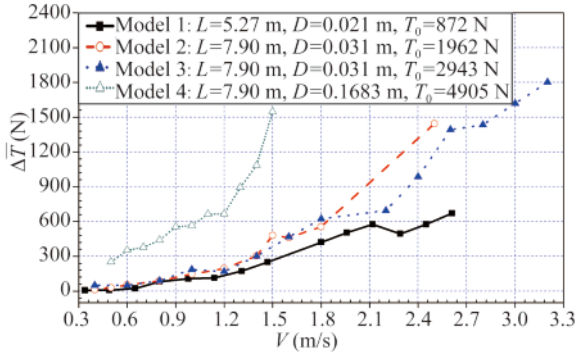

Fig. 8. Increment of the mean tension as a function of the current speed for Models 1–4.

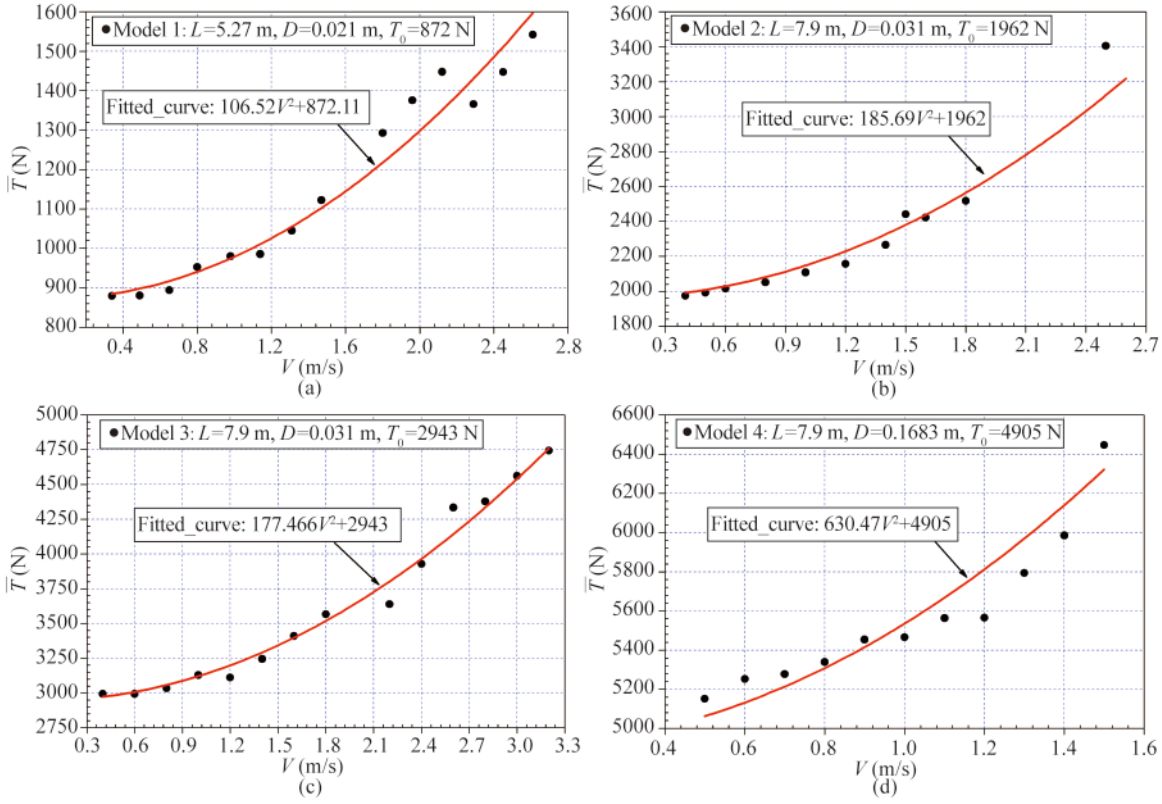

Fig. 7. Mean tension as a function of the current speed for Models 1–4; the fitted curve is obtained by using the least-squares method.

As $\Delta\overline{T}$ is found to be proportional to the square of the incident current speed, with reference to the Morison equation, $\Delta\overline{T}$ can be expressed as:

$$\Delta\overline{T} = \frac{1}{2}\rho C_{\mathrm{T}} D V^2, \tag{18}$$

where C_{T} is the tension coefficient. If C_{T} is known, $\Delta\overline{T}$ can be calculated. C_{T} is given by Eq. (19):

$$C_{\mathrm{T}} = \frac{2\Delta\overline{T}}{\rho D V^2}. \tag{19}$$

The tension coefficient (C_{T}) is presented as a function of Reynolds number in Fig. 9 for the four model tests. Re ranges from 6.014×10^3 to 2.158×10^5, showing that the flow field in all the tests was in the sub-critical regime.

Fig. 9 shows that C_{T} varies with the change of Reynolds number. This is mainly because the flow characteristics and the flow separation modes are strongly correlated with Reynolds number (Morse and Williamson, 2009), which further leads to different VIV responses and therefore different tension variation under different Reynolds numbers. The least-squares method is used to obtain the trend line shown in Fig. 9, which shows that C_{T} increases rapidly from 6 to 10 for $Re<2\times10^4$ and remains between 10 and 12 for $2\times10^4<Re<8\times10^4$. For $Re>8\times10^4$, C_{T} slowly decreases to 6 with the increasing Reynolds number. Thus, C_{T} varies between 6 and 12 over the full range of $6.014\times10^3<Re<2.158\times10^5$.

As shown in Fig. 9, C_{T} varies between 6 to 12 over the entire sub-critical Reynolds number regime. The top tension on the risers under a current can be estimated by using Eq. (19) and C_{T} from Fig. 9 to obtain more reliable estimates of the natural frequencies, VIV responses and stress distributions.

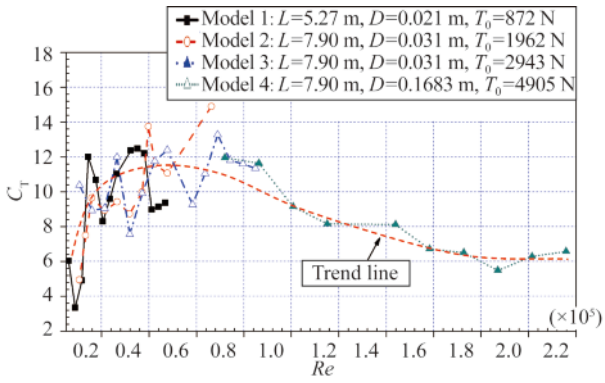

Fig. 9. Tension coefficient as a function of Reynolds number: the dashed trend line is obtained using the least-squares method.

4.2 Mean drag force distribution

Figs. 10 and 11 show the distribution of the normalized root mean square of the VIV displacement in the CF direction (Y_{RMS}/D), the mean bending strain in the IL direction $\overline{\varepsilon}_{\mathrm{mb}}(z)$ and the mean drag force $F_{\mathrm{md}}(z)$ for Models 3 and 4, respectively, along their normalized axial lengths.

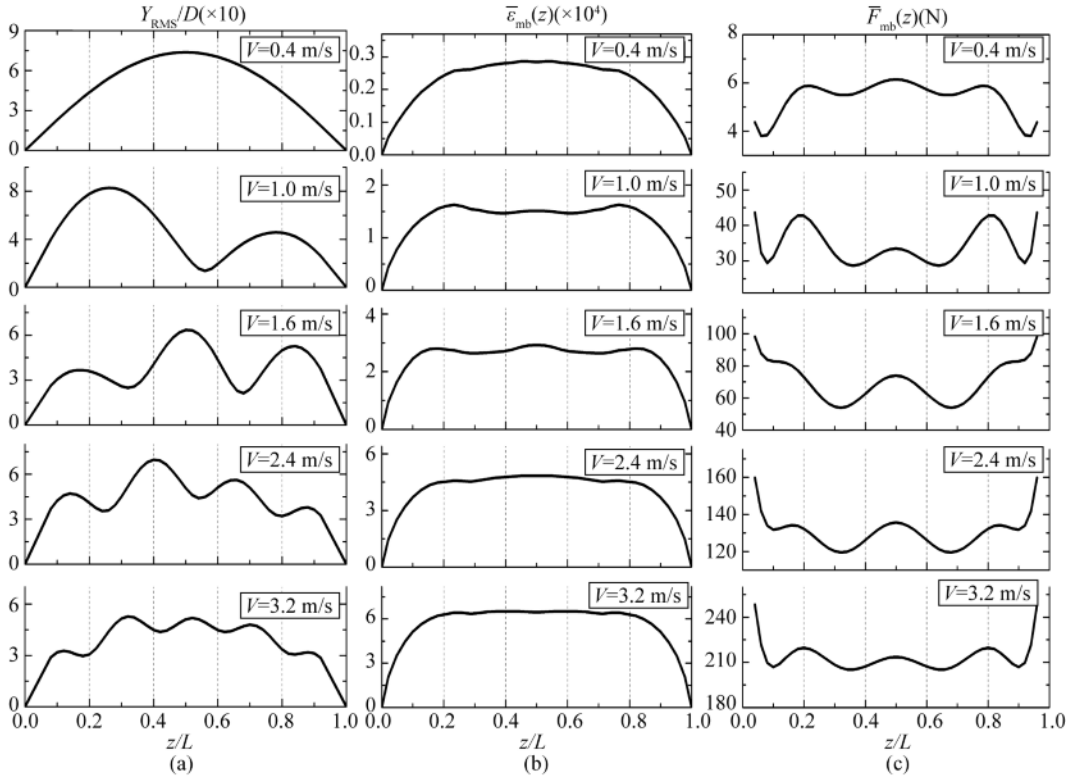

Fig. 10. Distribution of the normalized root mean square of the displacement of VIV in the CF direction, the mean bending strain, and the mean drag force along the axial direction for Model 3.

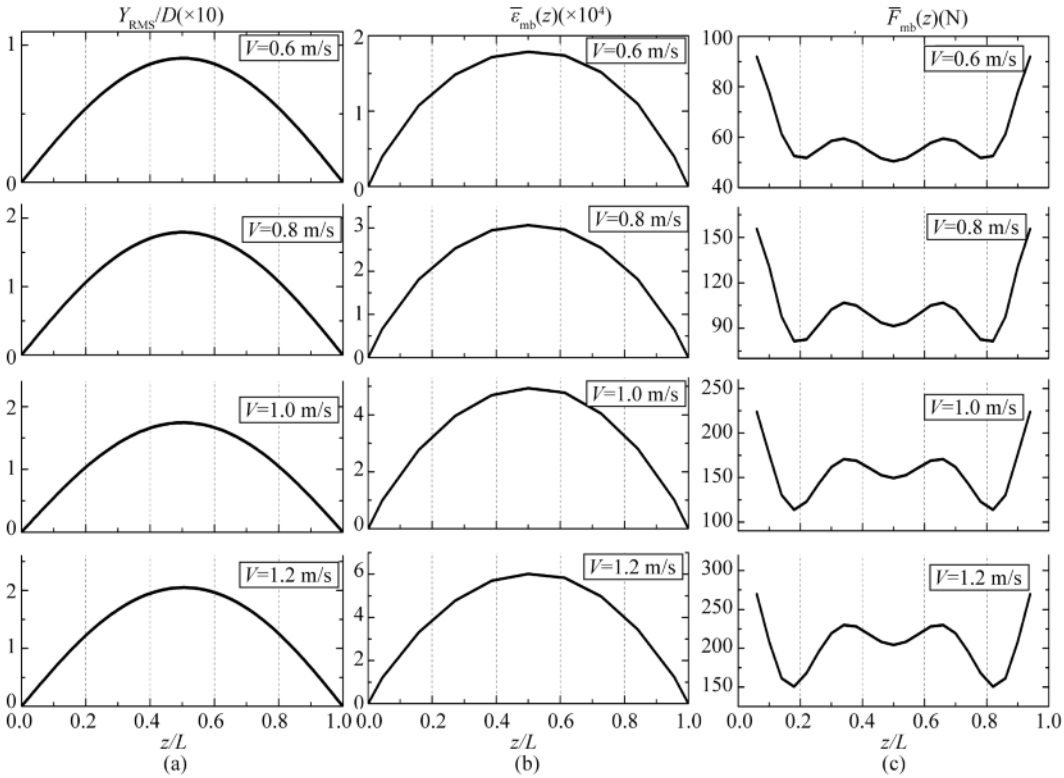

Fig. 11. Distribution of the normalized root mean square of the displacement of VIV in the CF direction, the mean bending strain, and the mean drag force along the axial direction for Model 4.

The dominant modes for the VIV in the CF direction are Mode 1, Mode 2, Mode 3, Mode 4, and Mode 5 for Model 3 at current speeds of 0.4, 1.0, 1.6, 2.4, and 3.2 m/s, respectively (Fig. 10a). For Model 4, Mode 1 is dominant for all the tested current speeds (Fig. 11a).

The mean drag force $\bar{F}_{md}(z)$ increases with the current speed (Figs. 10c and 11c), which leads to increasing $\overline{\varepsilon}_{mb}(z)$ (Figs. 10b and 11b). Furthermore, $\bar{F}_{md}(z)$ is distributed fairly uniformly along the model's axis and is symmetric about the midpoint of the axis. The larger the dominant VIV mode in the CF direction is, the more uniform the distributions of Y_{RMS}/D and $\overline{\varepsilon}_{mb}(z)$ are.

4.3 Drag coefficient distribution under VIV

The local drag coefficient $C_d(z)$ and the mean drag coefficient $\overline{C}_d$ can be obtained by using Eqs. (7) and (8) and the calculated $\overline{F}_{md}(z)$ for the models. In the tests performed on Model 4, two three-component force transducers are used at the ends of the model to measure the total drag force on the model, from which $\overline{C}_d$ can be directly obtained. The value of $\overline{C}_d$ calculated using Eq. (8) and the corresponding measured values at different current speeds are shown in Fig. 12 for Model 4. There is a good agreement between the calculated and measured values, with the maximum relative error of 2.618%. This shows that the method used to calculate the mean drag force on the models is reliable. Fig. 13 shows $\overline{C}_d$ for Models 1–4 as a function of Reynolds number.

Vandiver (1983) found that $\overline{C}_d$ can exceed 3 under VIV lock-in conditions in a steady uniform current for $Re<$

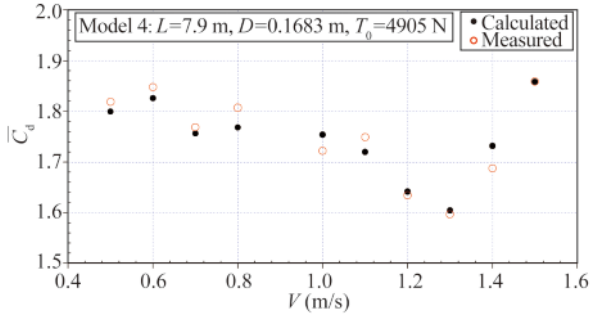

Fig. 12. Mean drag coefficient for Model 4 under different currents.

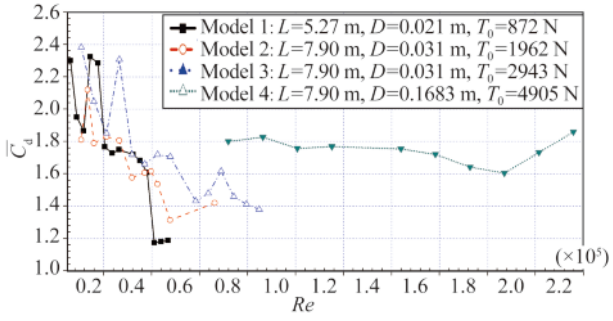

Fig. 13. Mean drag coefficient for different Reynolds numbers for Models 1–4.

2.2×10^4. Chaplin et al. (2015) found $\overline{C}_d$ values of 1.6–2.7 under stepped current conditions for $2.8\times10^3<Re<2.8\times10^4$. Fig. 13 shows that for $6\times10^3<Re<3\times10^4$, the values of $\overline{C}_d$ for Models 1–3 are between 1.7 and 2.4 (Fig. 12), which is in a good agreement with the results reported by Vandiver (1983) and Chaplin et al. (2005).

The mean drag coefficient values for Models 1–3 are generally larger than 1.4 for $Re<8\times10^4$ (Fig. 13). For Model 4, when Re increases to 2.2×10^5, $\overline{C}_d$ is still larger than 1.6. This result indicates that at high Reynolds number, $\overline{C}_d$ for flexible risers under VIV may still be much larger than 1.2 (the drag coefficient for a rigid cylinder in a current).

Models 2 and 3 are exactly the same except for the pre-tension at their two ends. Fig. 13 shows that $\overline{C}_d$ for Model 3 is larger than that for Model 2, showing that $\overline{C}_d$ depends significantly on the tension forces on the riser. The difference in the drag coefficient could be attributed to the effect of the pre-tension on the VIV for the models.

4.4 Predicted drag coefficient

Fig. 14 shows $\overline{C}_d$ and the corresponding VIV dominant mode numbers (N_d) in the CF direction under different current speeds for the four models. The mean drag coefficient ($\overline{C}_d$) depends strongly on N_d: as the current speed increases, N_d increases step-wisely, whereas $\overline{C}_d$ decreases. At different current speeds, the same N_d results in almost the same $\overline{C}_d$. When N_d changes from 1 to 2, $\overline{C}_d$ remains roughly the same. Especially for the cases of Model 4, a constant N_d, i.e., 1, results in $\overline{C}_d$ being roughly constant at different current speeds.

Vandiver used experimental data to develop a prediction model for the drag coefficient of a flexible riser under VIV (Vandiver, 1983):

$$C_d(z) = C_{do}\left[1 + 1.043\,(2Y_{RMS}/D)^{0.65}\right], \tag{20}$$

where $C_d(z)$ is the local drag coefficient at various cross-sections of the riser. C_{do} is the drag coefficient for a stationary cylinder, which is usually taken to be 1.2 in the subcritical Reynolds number regime.

Since the relationship between the mean drag coefficient ($\overline{C}_d$) and the dominant mode number (N_d) of the VIV in the CF direction, N_d is substituted into Eq. (20) to obtain a new prediction model for the drag coefficient on risers under VIV. Furthermore, by using the experimental results at high Reynolds number, two new parameters, the current speed (V) and the dominant frequency of VIV in the CF direction (f_{ex}) are also introduced to obtain the following empirical prediction:

$$C_d(z) = C_{do}\left[1 + \frac{0.16}{\sqrt{N_d}}\frac{V}{f_{ex}D}\,(2Y_{RMS}/D)^{0.65}\right]. \tag{21}$$

By averaging $C_d(z)$ at different axial positions on the models by Eq. (8), the predicted value of $\overline{C}_d$ under VIV at different current speeds can be obtained. Fig. 15 shows the measured $\overline{C}_d$ value for each model at different Reynolds numbers along with the predicted values that are obtained using Vandiver's formula Eq. (20) and Eq. (21).

Fig. 15 clearly shows that the measured value of $\overline{C}_d$ varies between 2.4 and 1.4 for different Reynolds numbers, showing that VIV amplifies the drag force. In general, $\overline{C}_d$ decreases as Reynolds number increases.

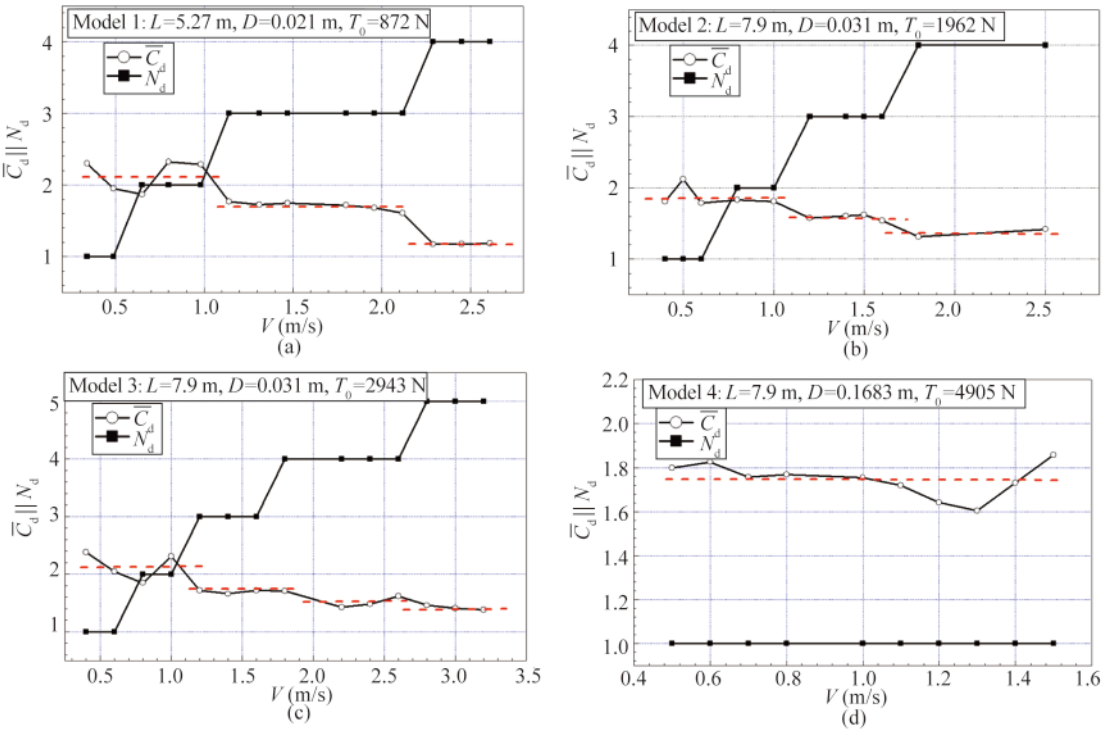

Fig. 14. Mean drag coefficient and corresponding VIV dominant mode number in the CF direction for Models 1–4 at different current speeds.

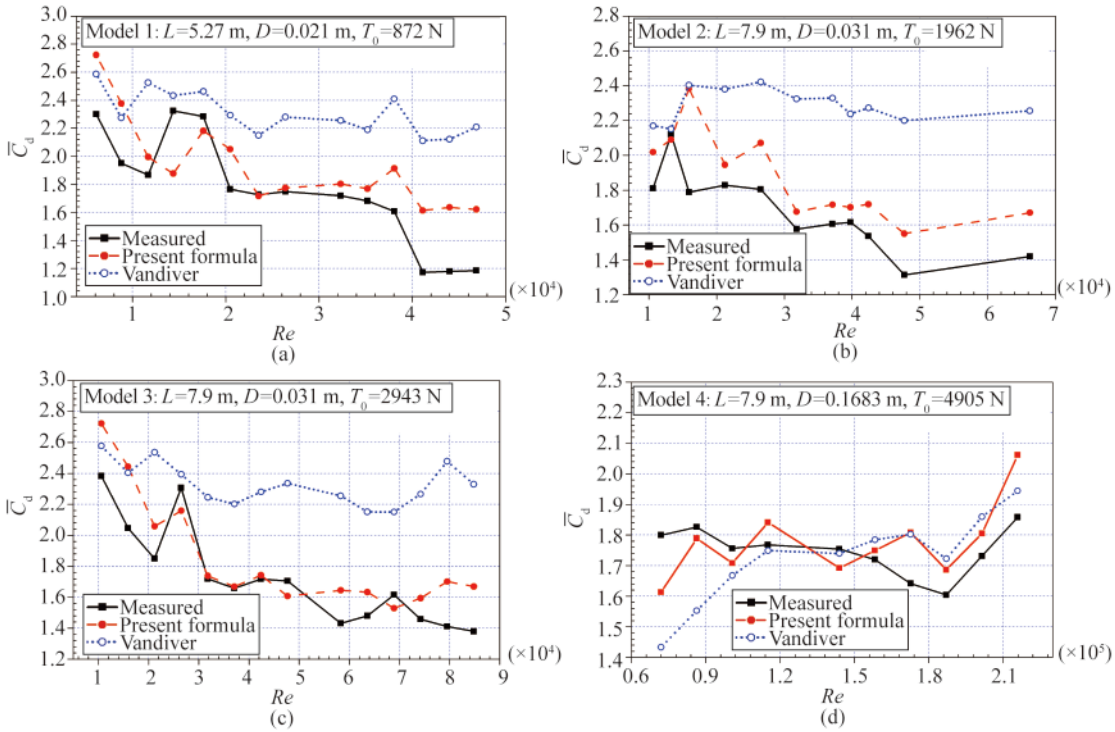

Fig. 15. Mean drag coefficients obtained usingVandiver's formula Eq. (20) and the proposed formula Eq. (21) together with the corresponding measured values under different Reynolds numbers for (a) Model 1, (b) Model 2, (c) Model 3, and (d) Model 4.

For $Re<2\times10^4$, the test results are very close to those predicted by Eq. (20); however, for $Re>2\times10^4$, the difference between the measured and predicted values increases significantly. The reason for this difference may be that Eq. (20) was developed and fitted for model test results with $Re<2.2\times10^4$, while the maximum Reynolds number in this study is considerably larger than 2×10^4. It is well known that Reynolds number significantly affects flow separation modes and hydrodynamic forces. For $Re<300$, the wake flow is laminar, and the flow pattern gradually becomes turbulent as Reynolds number increases. When Reynolds number is in the critical and super-critical regimes, the wake pattern becomes even more disordered. The boundary layer around the cylinder becomes asymmetric with laminar and turbulent sections, resulting in different hydrodynamic forces than those in the subcritical regions. This behavior could explain why Vandiver's formula (which was developed using experimental data for Reynolds number on the order of 10^4) does not accurately predict the drag coefficients of the riser under high Reynolds number on the order of 10^5 investigated in this study.

At lower Reynolds number, Eq. (20) generally predicts the drag coefficients for the models very well; however, the difference between the measured and predicted results increases with Reynolds number, and Eq. (20) generally over predicts the results for higher Reynolds number. However, Eq. (21) can predict the drag coefficients for the models very well for all the Reynolds numbers tested.

5 Conclusions

In this study, strain measurements using FBG strain sensors in the IL direction of the four riser models are used to determine the properties and distributions of the tension and drag forces for flexible risers under VIV in a uniform flow for Reynolds number up to 2.2×10^5.

The experimental results show that under uniform current conditions, the mean tension force is proportional to the square of the incoming current speed, and the tension coefficient of a flexible riser undergoing VIV is between 6 and 12. The tension coefficient analyzed can be helpful for the design of top-tensioned risers, flexible risers, and umbilicals.

The mean drag force is uniformly and symmetrically distributed along the axis of the risers undergoing VIV. The corresponding drag coefficient varies between 1.6 and 2.4 and does not equal a constant value of 1.2, as it does for a fixed cylinder in the absence of VIV.

These experimental results obtained for high Reynolds number on the order of 10^5 are used to develop a new empirical prediction model to estimate the drag force coefficients of flexible risers undergoing VIV, which accounts for the effects of the incoming current speed, the VIV dominant model number and the frequency. The new empirical prediction model can be used to predict riser's drag coefficients under VIV more accurately at high Reynolds number up to 2.2×10^5.

References

API RP 2RD, 1998. *Design of Risers for Floating Production Systems*

(*FPSs*) *and Tension Leg Platforms* (*TLPs*), American Petroleum Institute, Washington, DC.

Blevins, R.D., 1990. *Flow-Induced Vibration*, Van Nostrand Reinhold, New York.

Baarholm, R., Kristiansen, T. and Lie, H., 2007. Interaction and clashing between bare or straked risers: Analyses of experimental data, *Proceedings of the 26th International Conference on Offshore Mechanics and Arctic Engineering*, San Diego, USA, 3, 803–812.

Chaplin, J.R., Bearman, P.W., Huera-Huarte, F.J., and Pattenden, R.J.,2005. Laboratory measurements of vortex-induced vibrations of avertical tension riser in a stepped current, J. Fluid. Struct., 21(1),3–24.

Chen, T. and Chen, B., 1984. *Structural Mechanics for Ships*, National Defence Industrial Press, Beijing, 29–30. (in Chinese)

De Wilde, J.J. and Huijsmans, R.H., 2004. Laboratory investigation of long riser VIV response, *Proceedings of the 14th International Offshore and Polar Conference*, Toulon, France, 511–516.

Evangelinos, C., Lucor, D. and Karniadakas, G.E., 2000. DNS-derived force distribution on flexible cylinders subject to vortex-induced vibration, *J. Fluid. Struct.*, 14(3), 429–440.

Fang, S.M., Niedzwecki, J.M., Fu, S.X., Li, R.P. and Yang, J.M., 2014. VIV response of a flexible cylinder with varied coverage by buoyancy elements and helical strakes, *Mar. Struct.*, 39, 70–89.

Fang, S.M., 2013. *Structural Response Evaluation Using Non-uniform Sensor Arrays*, Ph.D. Thesis, Texas A&M University.

Fu, S.X., Ren, T., Li, R.P. and Wang, X.F., 2011. Experimental investigation on VIV of the flexible model under full scale Re number, *Proceedings of the 30th International Conference on Ocean*, *Offshore and Arctic Engineering* (*OMAE 2011*), Rotterdam, the Netherlands, Paper No. OMAE2011–49042.

Fu, S.X., Wang, J.G., Baarholm, R., Wu, J. and Larsen, C.M., 2013a. VIV of flexible cylinder in oscillatory flow, *Proceedings of the 32nd International Conference on Ocean*, *Offshore and Arctic Engineering* (*OMAE 2013*), Nantes, France, Paper No. OMAE2013–10348.

Fu, S.X., Wang, J.G., Baarholm, R., Wu, J. and Larsen, C.M., 2013b. Features of vortex-induced vibration in oscillatory flow, *J. Offshore Mech. Arct. Eng.*, 136(1), 011801.

Gao, Y., Fu, S.X., Ma, L.X. and Chen, Y.F., 2014. Experimental investigation of the response performance of VIV on a flexible riser with helical strakes, *Ships and Offshore Structures*, 11(2), 113–128.

Huera-Huarte, F.J. and Bearman, P.W., 2009. Wake structures and vortex-induced vibrations of a long flexible cylinder—part 2: Drag coefficients and vortex modes, *J. Fluid. Struct.*, 25(6), 991–1006.

Huera-Huarte, F.J., Bearman, P.W. and Chaplin, J.R., 2006. On the force distribution along the axis of a flexible circular cylinder undergoing multi-mode vortex-induced vibrations, *J. Fluid. Struct.*, 22(6), 897–903.

Li, L., Fu, S.X., Yang, J.M., Ren, T. and Wang, X.F., 2011. Experimental investigation on vortex-induced vibration of risers with staggered buoyancy, *Proceedings of the 30th International Conference on Ocean*, *Offshore and Arctic Engineering* (*OMAE 2011*), Rotterdam, the Netherlands, Paper No. OMAE2011–49046.

Morse, T.L. and Williamson, C.H.K., 2009. The effect of Reynolds number on the critical mass phenomenon in vortex-induced vibration, *Phys. Fluids*, 21, 045105.

Niedzwecki, J.M. and Fang, S.M., 2013. Suppression of flow-induced vibrations using ribbon fairings, *International Journal of Computational Methods and Experimental Measurements*, 1(4), 395–405.

Sumer, B.M. and Fredsoe, J., 2006. *Hydrodynamics Around Cylindrical Structures*, World Scientific, Singapore, 2–70.

Tognarelli, M.A., Slocum, S.T., Frank, W.R. and Campbell, R.B., 2004. VIV response of a long flexible cylinder in uniform and linearly sheared currents, *Offshore Technology Conference*, Houston, Texas, USA, OTC Paper No. 16338.

Vandiver, J.K., 1983. Drag coefficients of long flexible cylinders, *Offshore Technology Conference*, Houston, Texas, USA, OTC Paper No. 4490.

Wang, J.G., Fu, S.X. and Baarholm, R., 2014a. Vortex-induced vibration of steel catenary riser under vessel motion, *Proceedings of the 33rd International Conference on Ocean*, *Offshore and Arctic Engineering* (*OMAE 2014*), San Francisco, California, USA, Paper No. OMAE2014–23584.

Wang, J.G., Fu, S.X., Baarholm, R., Wu, J. and Larsen, C.M., 2014b. Fatigue damage of a steel catenary riser from vortex-induced vibration caused by vessel motions, *Mar. Struct.*, 39, 131–156.

Wang, J.G., Fu, S.X., Baarholm, R., Wu, J. and Larsen, C.M., 2015. Fatigue damage induced by vortex-induced vibrations in oscillatory flow, *Mar. Struct.*, 40, 73–91.

Willden, R.H.J. and Graham, J.M.R., 2001. Numerical prediction of VIV on long flexible circular cylinders, *J. Fluid. Struct.*, 15(3), 659–669.

Yamamoto, C.T., Meneghini, J.R., Saltara, F., Fregonesi, R.A. and Ferrari Jr., J.R., 2005. Numerical simulations of vortex-induced vibration on flexible cylinders, *J. Fluid. Struct.*, 19(4), 467–489.